metals

MDPI

Article

Effect of Quench Tempering on Hydrogen Embrittlement and Corrosion Behavior of X100 Pipeline Steel

Reza Khatib Zadeh Davani [1], Mohammad Ali Mohtadi-Bonab [2,*], Sandeep Yadav [1], Ehsan Entezari [1], Jhon Freddy Aceros Cabezas [3] and Jerzy Szpunar [1]

[1] Department of Mechanical Engineering, University of Saskatchewan, 57 Campus Drive, Saskatoon, SK S7N 5A9, Canada
[2] Department of Mechanical Engineering, University of Bonab, Bonab 5551395133, Iran
[3] Metallurgical Engineering and Materials Science Department, Universidad Industrial de Santander, Bucaramanga 680002, Colombia
* Correspondence: m.mohtadi@ubonab.ac.ir; Tel.: +98-413-774-5000

Abstract: In this study, the hydrogen embrittlement and corrosion behavior of X100 pipeline steel (Ref) was investigated after various heat treatments, including one-step austenitizing at 880 °C (HT3), 830 °C (HT2), and 780 °C (HT1) for 90 min, oil quenching to room temperature, tempering at 600 °C for 30 min, and air cooling to room temperature. Potentiodynamic polarisation was performed to assess the electrochemical corrosion behavior, while the Charpy impact test and Vickers microhardness measurement were performed to assess the hydrogen embrittlement susceptibility before and after hydrogen charging. SEM, EBSD, and EDS were used to further characterize the fractured surface and crystallographic texture of specimens, while XRD was used to evaluate the macro-texture and corrosion products. The results of the Charpy impact and hardness tests showed that the high hardness and low impact energy values in the Reference and HT3 specimens were linked to a higher susceptibility to hydrogen embrittlement, indicating that the hardness values and Charpy impact energy, respectively, increased and decreased with a decrease in the hydrogen embrittlement resistance. The micro-texture results from the EBSD analysis showed that the HT3 and Ref. specimens had higher Kernel average misorientation (KAM) values and higher deformed grains fractions than those of the HT2 and HT1 specimens, resulting in lower corrosion resistance. The HT2 specimen had an optimal combination of beneficial ({110}, {111}, {332}) and harmful texture components ({100}), showing that corrosion resistance can be improved.

Keywords: quench tempering; hydrogen embrittlement; Charpy test; corrosion resistance; EBSD; XRD

Citation: Khatib Zadeh Davani, R.; Mohtadi-Bonab, M.A.; Yadav, S.; Entezari, E.; Cabezas, J.F.A.; Szpunar, J. Effect of Quench Tempering on Hydrogen Embrittlement and Corrosion Behavior of X100 Pipeline Steel. *Metals* **2023**, *13*, 841. https://doi.org/10.3390/met13050841

Academic Editors: John Campbell and Claudio Pistidda

Received: 14 March 2023
Revised: 9 April 2023
Accepted: 21 April 2023
Published: 25 April 2023

1. Introduction

Building infrastructures for hydrogen transport is important for a future hydrogen-based economy. Large amounts of hydrogen can be transported across long distances using pipelines [1–4]. Since pipelines are used in sour environments, they are subjected to hydrogen embrittlement and corrosion damage. Hydrogen embrittlement poses a significant risk to the safe operation of pipelines with cathodic protection, since it might result in sudden and unpredictable pipeline failures [5–7]. At the end of the 19th century, Johnson [8] pointed out that hydrogen embrittlement changes the mechanical characteristics of steel. The elongation to failure is lowered significantly, while the yield stress and final strength remain unaffected. This condition is also linked to a decrease in fracture resistance. Zhang et al. [9] observed that hydrogen embrittlement at crack tips promotes the transition from a ductile fracture to a brittle fracture. Many researchers have claimed that hydrogen embrittlement is associated with several mechanisms, including (1) the weakening of metal atomic bonds; (2) the enhanced deterioration of plasticity; (3) hydrogen-enhanced decohesion; and (4) adsorption-induced dislocation emissions [5,10,11].

Hydrogen and corrosion damages in pipeline steels are affected by harsh operational conditions, such as high pressures, the environment chemistry (pH and relative humidity), corrosive agents (H_2, CO_2, H_2S, O_2), and residual or applied stress, all of which are responsible for different hydrogen-related damage mechanisms [4,12–14]. Hydrogen-induced cracking (HIC) is the most prominent type of damage in a sour environment. The hydrogen created by pipe corrosion on the surface diffuses into the steel and accumulates at defect sites, such as inclusions, precipitations, phase interfaces, martensite islands, and grain boundaries. The hydrogen atoms recombine to create hydrogen molecules, causing the internal pressure to build up inside the cracks and other openings. This causes hydrogen embrittlement, which lowers the ductility and toughness of pipeline steels [15–17].

Replacing hydrogen-damaged pipelines is not economical, so there is a need to develop a novel approach to engineer steels that are less susceptible to HIC. Several methods for controlling and minimizing hydrogen embrittlement and corrosion damage in pipeline steel have been used, including coatings, desulphurization, inclusion control, and microstructure and crystallographic texture control [16,18,19]. To modify the microstructure and texture of pipeline steel, thermomechanical control processing (TMCP) parameters, such as hot rolling as well as the heating and cooling rate, can be considered [20–22]. Pourazizi et al. [1] reported that quenching API 5L pipeline steel with a higher cooling rate decreased the grain size, which led to less resistance of the steel to HIC cracking. Fuchigami et al. [23] reported that decreases in temperature and time during the austenitizing process decrease the prior austenite grain size and enhance the HE resistance of X100 pipeline steels. Masoumi et al. [24] reported that a high level of HIC resistance was obtained in a specimen rolled isothermally at 850 °C, due to the higher amount of grains oriented with {110} planes. On the other hand, several researchers have tried to establish a correlation between crystallographic orientation and anodic dissolution [25–28]. In a study conducted on API 5L pipeline steel in order to determine the effect of thermochemical processing, it was discovered that the corrosion rate was lower in the specimen that was charged with hydrogen as compared to another that was not charged [29]. Moreover, another study also showed that the specimen that was cooled faster had higher corrosion resistance [29]. Ohaeri et al. [30] investigated the effect of different rolling temperatures at 700 °C, 600 °C, and 500 °C on corrosion resistance and discovered that anodic dissolution was increased in the order of 700 °C > 600 °C > 500 °C for hydrogen and non-hydrogen test media. Venegas et al. [31] developed a novel model for describing the relationship between the crystallographic texture and corrosion behavior of API 5L steels. They found good agreement when they compared their predictions of the average corrosion resistance index based on the crystallographic texture with the data obtained from potentiodynamic polarization and electrochemical impedance spectroscopy (EIS) [31].

Another process that improves hydrogen embrittlement resistance is tempering. Tempering makes it possible to decrease the brittleness of martensite, dislocation density, and austenite grain stored energy, leading to the enhanced hydrogen embrittlement resistance of pipeline steels [2]. Hoschke et al. [32] showed that the tempering process enhanced the hydrogen embrittlement resistance of X100 pipeline steel by reducing the number of reversible hydrogen trapping sites, such as dislocations, and the residual stored energy surrounding austenite grains. Nevertheless, research on the correlation between anodic dissolution resistance and crystallographic texture is ongoing. Therefore, it is necessary to look for processing techniques that can eventually result in the development of corrosion-resistant steels. The electrochemical testing of pipeline steels for various applications has been the topic of several corrosion investigations. The effect of quench tempering on the hydrogen embrittlement and corrosion behavior of pipeline steel has received little attention.

This research study aims to evaluate the hydrogen embrittlement and corrosion behavior of X100 pipeline steel specimens subjected to several heat treatments (one-step austenitizing at 880 °C, 830 °C, and 780 °C, followed by quenching and tempering at 600 °C). The hydrogen embrittlement was examined using the Charpy and hardness tests. The corrosion behavior was examined using potentiodynamic polarisation and electro-

chemical impedance spectroscopy (EIS). The crystallographic texture, texture components, and corrosion products were evaluated using EBSD and XRD analyses.

2. Materials and Methods

Specimens of X100 pipeline steel used in this research had the chemical composition shown in Table 1. The thickness of the as-received pipeline steel (called Ref.) was 20 mm.

Table 1. Chemical composition of X100 pipeline steel (Wt.%).

C	Si	Mn	S	P	Ni	Cr	Mo	V	Cu	Al
0.06	0.25	1.7	0.001	0.015	0.143	0.016	0.19	0.004	0.24	0.02

The heat treatment process was performed according to three different patterns illustrated in Figure 1. According to Figure 1, the specimens were first austenitized at three different temperatures of 880 °C (for the specimen HT3), 830 °C (for the specimen HT2), and 780 °C (for the specimen HT1). The specimens stayed at the mentioned temperatures for 90 min and then they were oil quenched to room temperature. Finally, all quenched specimens were tempered to 600 °C for 30 min and were air-cooled to room temperature.

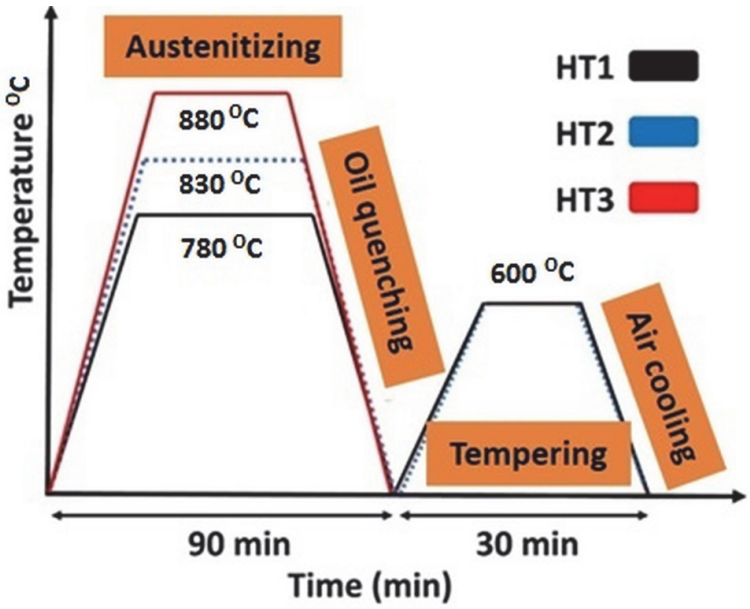

Figure 1. Schematic diagrams of the heat treatment process.

To evaluate the hydrogen embrittlement behavior of heat-treated specimens, the electrochemical hydrogen charging process was conducted on specimens with the dimension of 4 cm × 4 cm × 2 cm at current density of 20 mA/cm^2 for 24 h. The specimens were immersed in a sour environment into the hydrogen charging cell, including 1 wt% H_2SO_4 and 3 g/L NH_4SCN at a pH of 1.1, with an ambient temperature and pressure. The reason for using H_2SO_4 and NH_4SCN was to charge the specimen in sour environment and to avoid the depletion of the active component of the electrolyte solution during the cathodic charging test, respectively, which assists atomic hydrogen penetration into the specimen. Furthermore, the specimen acted as the cathode, while the platinum electrode acted as the anode, and both were connected to the current source in this experiment. After that, the specimens were used to perform the Charpy and Hardness tests. The Charpy impact test was conducted on an Instron Charpy tester machine (Instron, Norwood, MA, USA), according to the ASTM E23-07 standard. Each Charpy impact test was run three times to ensure the accuracy of the experimental data. A fractographic examination of the Charpy-tested specimens was performed, using a Hitachi SU6600 scanning electron microscope (SEM)

(Hitachi High-Tech Corporation, Tokyo, Japan) outfitted with an energy-dispersive X-ray spectroscopy (EDS) detector (Hitachi High-Tech Corporation, Tokyo, Japan). Further, the Vickers microhardness measurement was carried out using the MVK-H1 Mitutoyo Vickers hardness tester (Mitutoyo, Tokyo, Japan) set at 1 kg load. There were five indents on each specimen and the results show the average of the results obtained for each specimen.

The electrochemical response to a corrosive media for the heat-treated specimens was investigated, using the potentiodynamic polarization on the Gamry instrument interface 1000 Potentiostat/Galvanostat/ZRA. According to Figure 2, the experimental cell consists of a three-electrode system: the specimen as a working electrode, the saturated calomel electrode (SCE) as a reference electrode, and the graphite rod as a counter electrode. The test was performed at room temperature in the acidic media with 1 wt.% H_2SO_4 and 3 g/L NH_4SCN at a pH of 1.1. All the potentiodynamic polarization tests and electrochemical impedance spectroscopy (EIS) were carried out after the stabilized open-circuit potential (OCP) was reached. The electrochemical specimen masks included in the PTC1 kit aided in defining the 1 cm^2 working area on the specimens placed within the cell. The electrolytes used in this test were prepared in accordance with the NACE TM 0284-2016. After the corrosion test, the morphology of the corroded surface and corrosion products was examined using SEM and a Bruker D8 Discover X-ray diffractometer (XRD) (Bruker, Billerica, MA, USA), respectively.

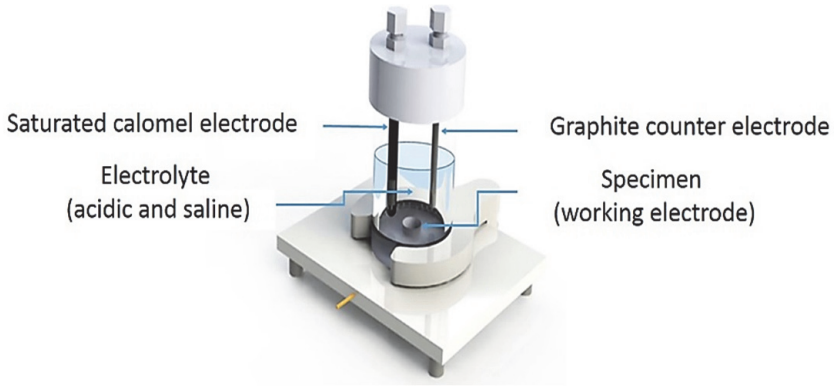

Figure 2. Schematic cell of corrosion test.

To evaluate the crystallographic orientation and the texture components and their link to corrosion behavior, the specimens first were cut from the top surface with a thickness of 2–4 mm and were pre-polished using 100 to 4000 SiC grit papers followed by final polishing with 3µm MD-mol and 1µm MD-Nap. Then, the crystallographic orientation of prepared specimens was measured using a Hitachi SU6600 scanning electron microscope (SEM) (Hitachi High-Tech Corporation, Tokyo, Japan) outfitted with EBSD. The texture components of studied specimens also were evaluated, using Bruker D8 Discover XRD (Bruker, Billerica, MA, USA) with an area detector system and Cr K radiation.

3. Results and Discussion

3.1. Mechanical Properties

Figure 3 presents the Charpy test results for the Ref., HT1, HT2, and HT3 specimens at room temperature. The applied heat treatments improved the impact energy values of all the tested steels by 40%; however, the HT2 specimen had the highest impact. This indicates that tempering at 600 °C was responsible for the increase in impact Charpy energy in both the uncharged and charged specimens. However, it is worth mentioning that the differences in the impact energy of all the heat-treated specimens were small. Further, the impact energy values in all steels were reduced by a range of 27 to 40% following electrochemical hydrogen charging.

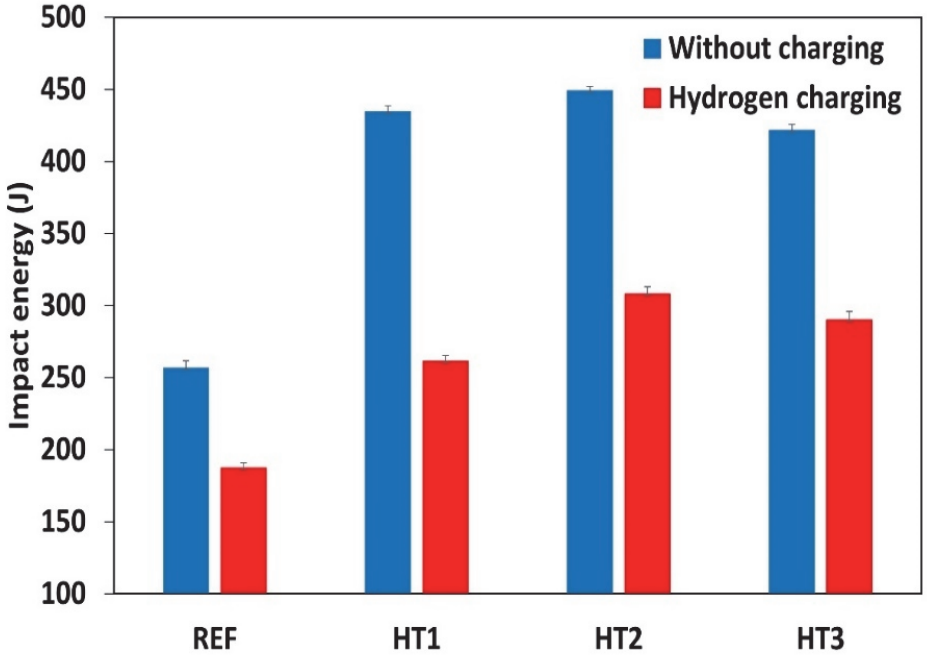

Figure 3. The results of the Charpy test at room temperature.

Figure 4a–d show the fracture surfaces of the Ref., HT1, HT2 and HT3 specimens not charged with hydrogen after he Charpy test. As shown in these figures, the fracture surface of the uncharged specimens had many dimples, which is a sign of a ductile fracture. However, in the case of the HT1 specimen, the dimples were shallower than those in the other uncharged specimens. It should be mentioned that both types of ductile and brittle fractures were also observed in the pipeline steel with no hydrogen charging [33,34]. However, the dominant mode of fracture of all the tested specimens after electrochemical hydrogen charging was brittle. Figure 4e–h show the fracture surfaces of the Ref., HT1, HT2, and HT3 hydrogen-charged specimens after the Charpy test. It is clear from these figures that there is a considerable difference between the specimens tested with and without hydrogen charging. Despite the fact that the fracture surfaces of the steels before hydrogen charging included more dimples, the fracture surfaces of the Charpy-tested specimens after hydrogen charging had a combination of dimples and quasi-cleavage, indicating evidence of hydrogen embrittlement in the hydrogen-charged specimens. Lee et al. [35] also found that the absorbed impact energy considerably decreased with the increase in the hydrogen charging time. They observed that the reduction in the impact energy was accompanied by cleavage fracturing with a noticeable decrease in the frequency of ductile dimples [35]. The findings of these researchers were consistent with our observations.

The red arrows on the fracture surfaces of the specimens after hydrogen charging are presented in Figure 4. The red rectangles mark the HIC cracks where the inclusions were observed near the HIC pathway, which indicates that the inclusions may have affected the HIC formation. Huang et al. [36] and Peng et al. [37] reported that HIC nucleated from inclusions; thus, the inclusions were recognized as hydrogen trapping sites with high residual stress, increasing the HIC susceptibility of pipeline steels. It is worth mentioning that the combined effect of the hydrogen buildup pressure and the externally applied stress in the Charpy experiment facilitated the propagation of cracks. Without external stresses, most HIC cracks initiate and propagate through the mid-thickness of the steel where there is segregation of some elements, such as Mn, S, Ca, Mg, and Ti. Moon et al. [38] implied that the segregation of the alloying elements often happens in the middle of the cross-section of the cast slab because of the well-known mechanism of solidification during casting. Therefore, hard phases are formed there and HICs nucleate in this region.

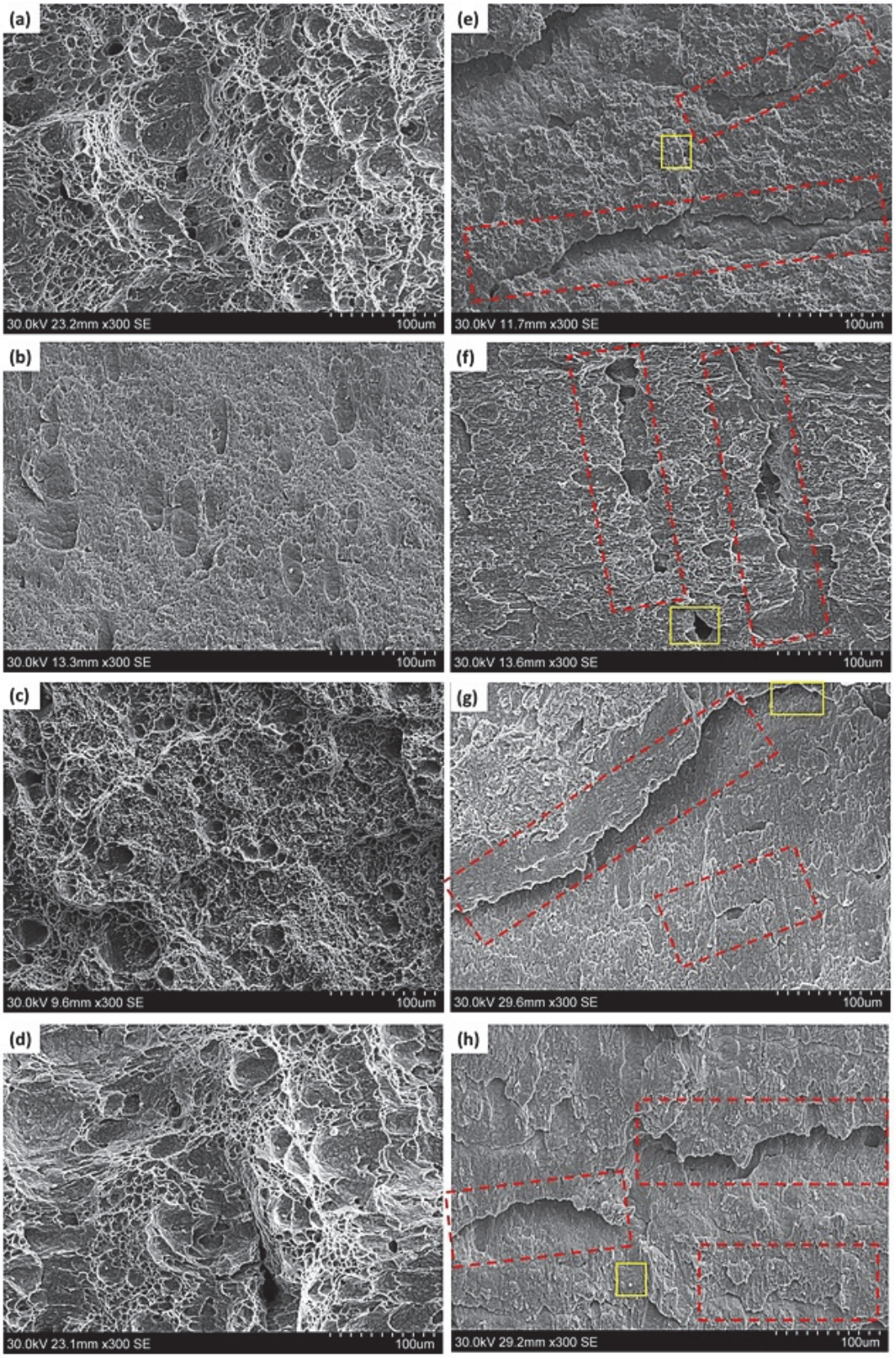

Figure 4. Fractography micro images of the Charpy specimens for pipeline steels without hydrogen charging: (**a**) Ref., (**b**) HT1, (**c**) HT2, (**d**) HT3; and after hydrogen charging: (**e**) Ref., (**f**) HT1, (**g**) HT2, (**h**) HT3. The red rectangles represent the HIC. The yellow rectangles represent the areas used for EDS analysis in Figure 5.

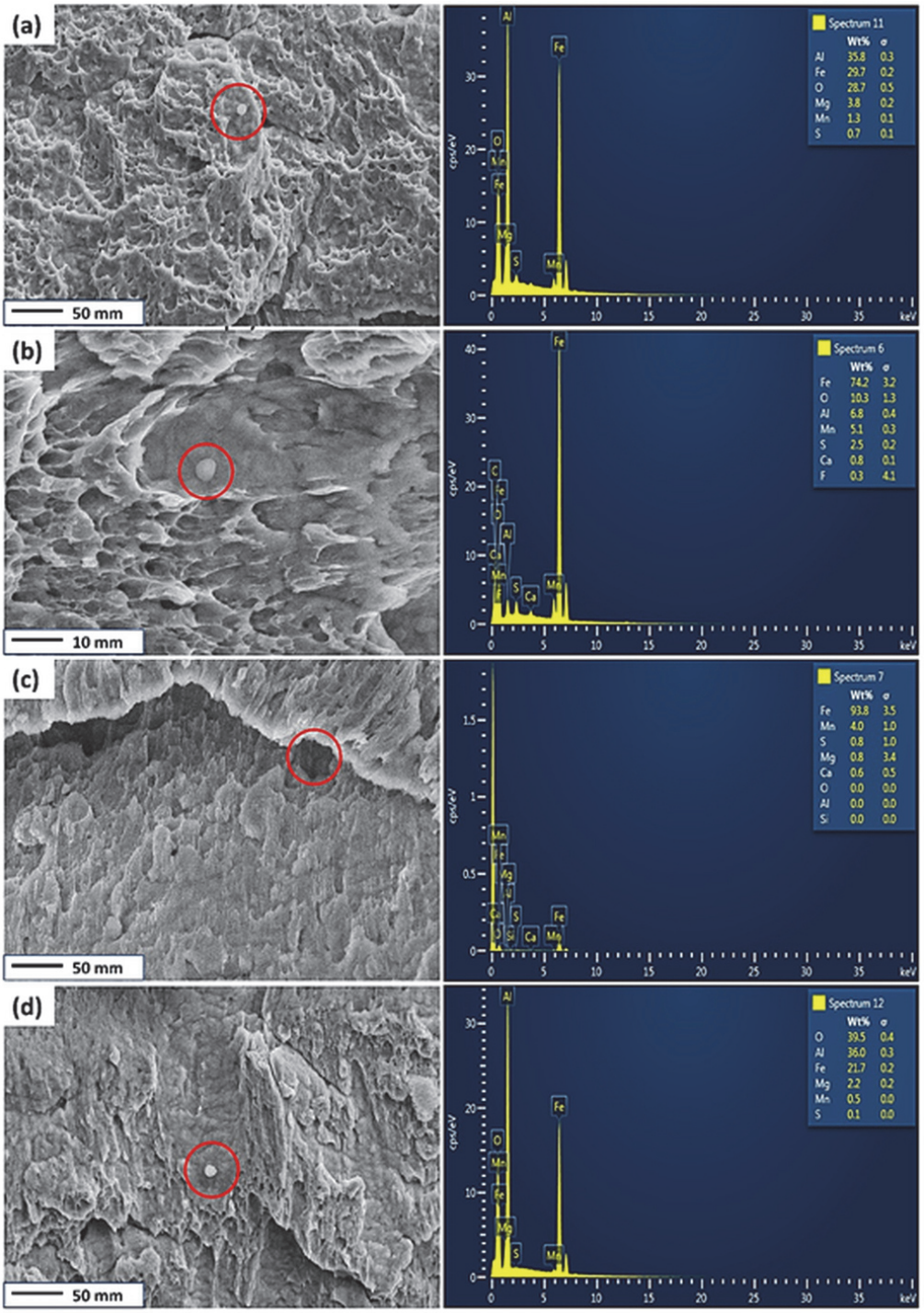

Figure 5. The EDS point spectrum of the inclusions around the HIC cracks (the yellow rectangles in Figure 4) for specimens after hydrogen charging (**a**) Ref., (**b**) HT1, (**c**) HT2, and (**d**) HT3. The red circles represent the site of inclusions.

Figure 5 shows the EDS point spectrum of the inclusions around the HIC cracks for the pipeline steels after hydrogen charging for the Ref., HT1, HT2, and HT3 steels. This image shows that some inclusions are observed in the microvoids of the fracture surface. As seen in the EDS scans, the Mn-, Al-, and S-based inclusions are seen on the fracture surface in the Ref., HT1, and HT3 steels after hydrogen charging. The Mn-, Al-, and S-based inclusions are susceptible to fracture initiation. Bigger inclusions containing Mn, Mg, and S are observed on the fractured surface of the HT2 specimen.

Figure 6 shows the microhardness of all the tested steels before hydrogen charging and after 24 h of hydrogen charging. One can see that the average hardness values in the Ref., HT1, HT2, and HT3 specimens increased by 11.5%, 7.7%, 6.1%, and 8% respectively, compared with the uncharged specimens, indicating the effect of hydrogen embrittlement. Based on the increments in the hardness value after hydrogen charging, the hydrogen embrittlement susceptibility was maximal in the Ref. and HT3 specimens, while it was lower in the case of the HT2 and HT1 specimens. Latifi et al. [39] also investigated the effect of electrochemical hydrogen charging on the hardness of API X65 pipeline steel. They noted that the micro-hardness of the steel was considerably increased after hydrogen pre-charging. The increase in the hardness value was related to the locking of dislocations in the presence of hydrogen. This phenomenon may be observed in other types of steel [39].

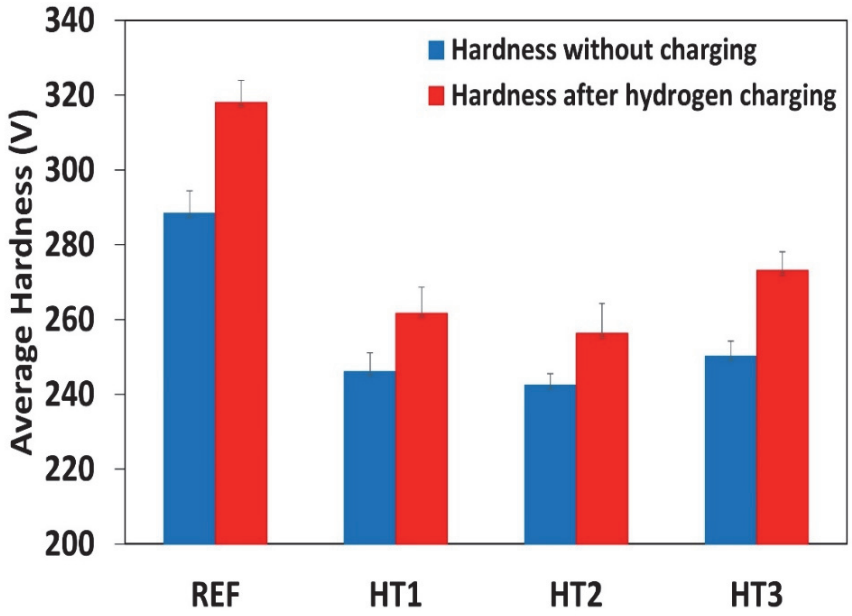

Figure 6. Microhardness of pipeline steels without hydrogen charging and after 24 h of hydrogen charging.

3.2. Corrosion Analysis and Texture Evolution

Figure 7a–c and Table 2 represent the results of the potentiodynamic polarization test and electrochemical impedance spectroscopy, including the OCP curve, Tafel curve, and Nyquist plot for all the Ref., HT1, HT2, and HT3 steels exposed to corrosive media. OCP is the potential created between the steel surface and the environment, with respect to a reference electrode. Figure 7a depicts the evolution of the OCP curves at various steel specimens submerged in a solution. In the Ref. specimen, the E_{OCP} started at −500 mV and then monotonically decreased, and the steady state was reached after 3600 s. This indicates that the Ref. specimen has a high level of corrosion activity in an acidic environment. In contrast, the OCP curve for the heat-treated specimen monotonically increases until it reaches a steady state, showing a decline in its activity in acidic media with time and hence, a better corrosion resistance than that of the Ref. specimen. However, when comparing their potential, the OCP curves for HT2 are comparatively shifted towards a less negative potential than those for HT1 and HT3, showing that the corrosion activity is significantly reduced in acidic environments. Further, compared to other heat-treated specimens, the HT3 specimen showed a more negative potential and hence a higher level of corrosion activity. The HT1 and HT3 specimens showed a significantly lower level of activity in acidic media, compared with that of the Ref. specimen. This behavior may be attributed to the higher tendency for passivation in the heat-treated specimen in corrosive media in contrast to the Ref. specimen. A similar behavior for the OCP has been reported in the past, in which the initial dissolution of bare steel in the air created an oxide film, reducing the corrosion trend [40].

Furthermore, the Tafel curves of the Ref. and heat-treated specimens were determined in the acidic media, as illustrated in Figure 7b. Typically, a Tafel curve is used to understand the interfacial reaction between the steel surface and the electrolyte. The electrochemical parameters were also extracted from the potentiodynamic polarization curves, as shown in Table 2. These parameters were calculated based on the Tafel extrapolation technique in which the corrosion rate was determined from the intersection of the linear portion of the Tafel curves (as shown in Figure 7b). In the Tafel curves, the anodic polarization curve is related to the anodic dissolution of the steel specimens, while the cathodic polarization curve shows the evolution of hydrogen caused by the reduction in water. The results extracted from the Tafel curves and shown in Table 2 indicated that the corrosion rate was almost twice as low in HT1 and HT2 compared to Ref. and HT3, indicating that the corrosion resistance was greatly enhanced by following the HT1 and HT2 heat treatment path. Moreover, when we compared Ref. and HT3, the corrosion resistance of HT3 was relatively lower in the acidic media.

The cathodic polarization curve reveals a linear Tafel zone, which corresponds to a constant reduction reaction rate. Additionally, an inflection point with two slopes is observed at a potential greater than the corrosion potential observed in the cathodic polarisation curves. This inflection point refers to the change in the mechanism of the cathodic reaction and may signify the formation of a protective layer or the activation of different reduction cations [41]. Afterward, the Nyquist curves were obtained from the EIS curves, as shown in Figure 4c. Typically an EIS test is used to understand the interfacial reaction between the steel surface and electrolyte. The Nyquist result indicated that the diameter of the impedance ring was the largest for HT2 and the smallest for HT3, as well as that the corrosion resistance was the highest for HT2 and the lowest for HT3. When steel samples are exposed to an electrolyte, the EIS test yields deflected half-circles, which can be attributed to surface irregularities or the control of charge transfer on the surface layers [42]. However, when comparing Ref. and HT1, HT1 exhibited a higher corrosion resistance than that of Ref. Overall, the EIS test results were consistent with the potentiodynamic polarization curve and OCP curve results, which indicated that the corrosion resistance of X100 steel can be significantly improved by performing the HT1 and HT2 heat treatments.

Table 2. Tafel parameters for steels in H media.

Specimen	Beta A (V/Decade)	Beta C (V/Decade)	I_{corr} (μA)	E_{corr} (mV)	Corossion Rate (mpy)
Ref.	27.7×10^{-3}	170.5×10^{-3}	12.3	−464	10.6
HT1	31.7×10^{-3}	113.7×10^{-3}	6.3	−481	3.9
HT2	24.8×10^{-3}	163.2×10^{-3}	5.9	−460	2.5
HT3	31.2×10^{-3}	109.3×10^{-3}	14.8	−493	15.6

An EBSD analysis was performed to link the corrosion behavior of the heat-treated specimens to the misorientation map, as seen in Figure 8a–d. In the legend of the KAM maps (Figure 8a–d), the numbers represent the intensity of local misorientation, with 0 being the smallest amount of local misorientation (Blue), 1–2 representing a moderate amount of local misorientation (greenish), and 3–5 indicating the greatest amount of local misorientation (yellow and reddish). The local misorientation maps revealed that the HT3 and Ref. steel specimens had higher kernel average misorientation (KAM) values than those of the HT2 and HT1 specimens, indicating that the corrosion resistance of the steels with greater amounts of misorientation was significantly reduced. This is due to the fact that the HT3 specimen was quenched from a high austenization temperature (880 °C) in the same quenching environment, resulting in a higher quenching rate for HT3 than for the other steels. Conversely, the grains had a lower amount of stored energy in the HT2 and HT1 specimens with a lower quenching rate from a lower austenization temperature, which might be responsible for the high corrosion resistance in acidic environments [26,30,43].

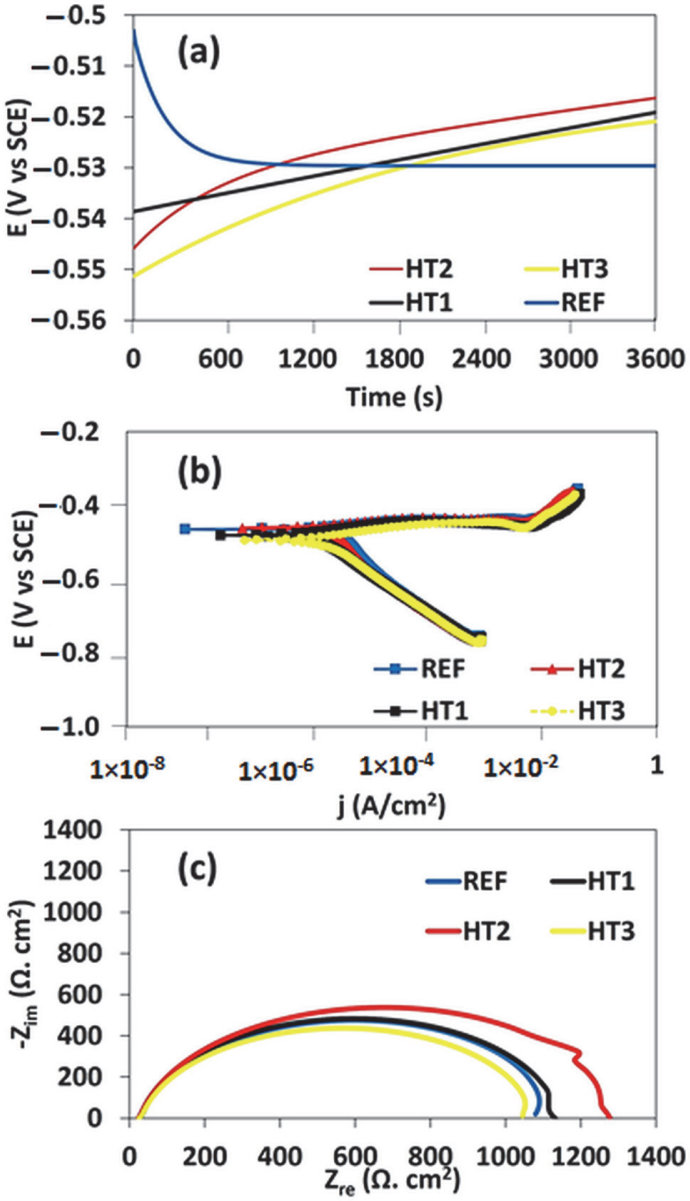

Figure 7. (**a**) E_{OCP} vs. time plot, (**b**) E Tafel curve, (**c**) Nyquist plot for steels in corrosive media.

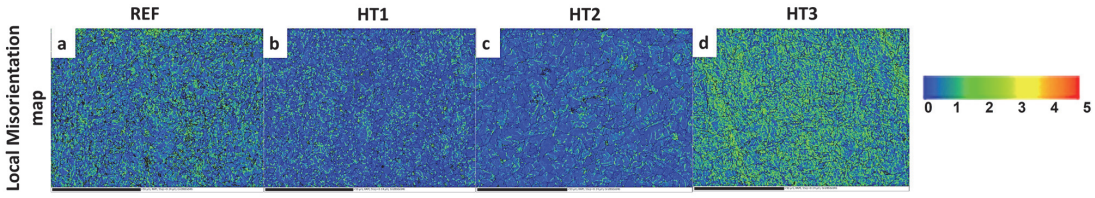

Figure 8. EBSD orientation map showing local misorientation maps in (**a**) REF, (**b**) HT1, (**c**) HT2, and (**d**) HT.

In addition, a bulk texture analysis was performed with the aid of X-ray diffraction to investigate the effect of the texture components on the corrosion behavior of the Ref. and heat-treated specimens, as demonstrated in Figure 9a–d. The orientation distribution functions (ODFs) were calculated from the {110} and {200} pole figures. The volume fraction of important texture components was also calculated as shown in Table 3. It is evident that texture intensities are relatively higher in Ref. and HT1 in contrast to HT2 and HT3. However, when comparing the volume fraction of the desired texture components {111}

and {332}, we can see that their volume fraction is increasing in the following order of specimens: Ref. < HT1 < HT2 < HT3. Another important grain orientation {110} exhibited the following trends: HT1 ≈ HT3 < HT2 ≈ Ref. Contrary to this, the volume fraction of undesired texture components, such as {100}, was found to have the following trend: HT2 < HT3 < HT1 ≈ Ref. Thus, the HT2 specimen had the optimal combination of beneficial ({110}, {111}, {332}) and harmful texture components ({100}), indicating a trend for the improvement in corrosion resistance.

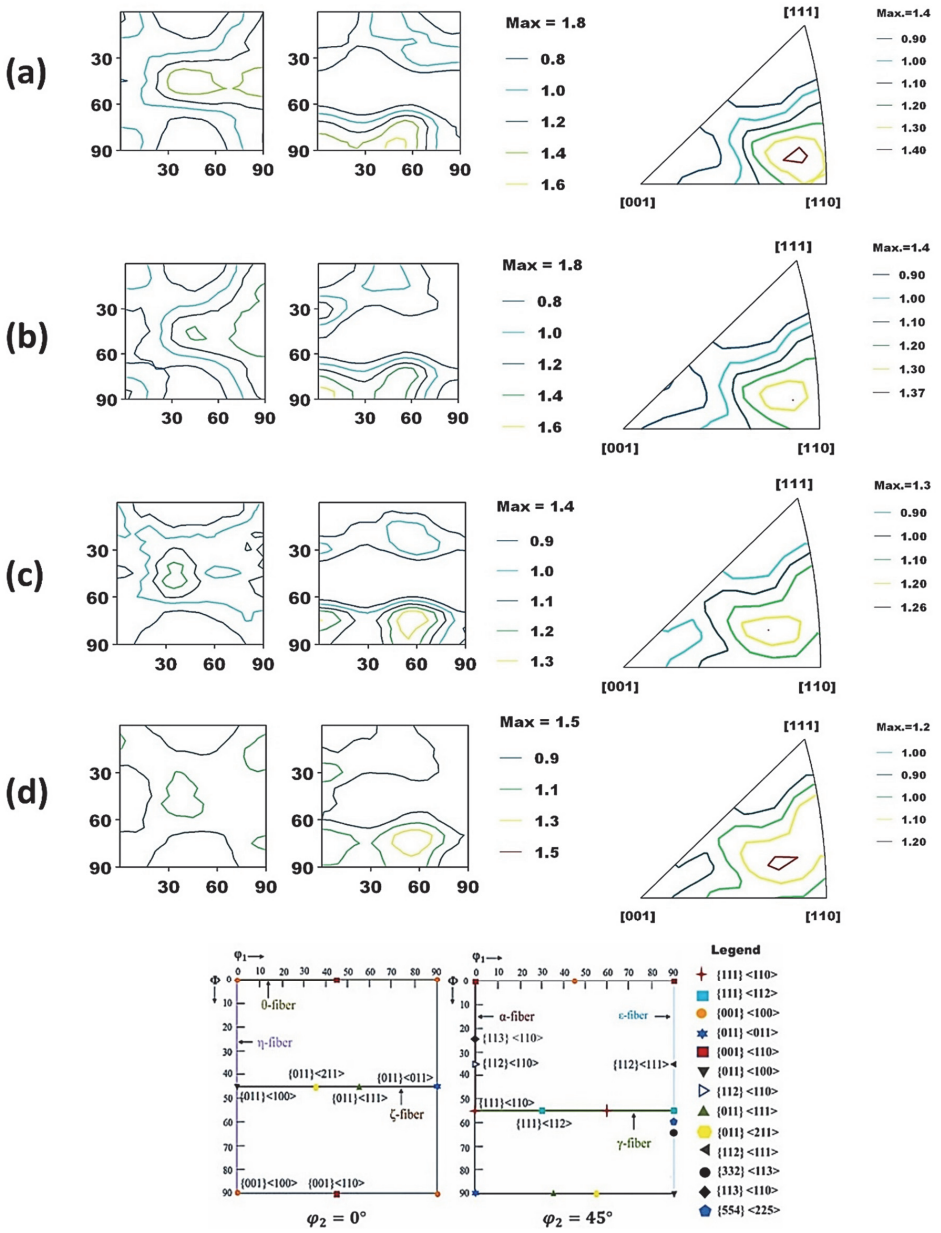

Figure 9. Orientation distribution function (ODF) map for (**a**) Ref. (**b**) HT1, (**c**) HT2, and (**d**) HT3. The attached schematic also represents the typical ideal texture components and fibers in BCC steels in φ2 = 0° and 45° sections of Euler space.

Moreover, an XRD analysis of the corrosion products on the corroded surface of the specimens was performed, as shown in Figure 10. As is clear in this figure, there is a predominant corrosion product: FeS. The FeS is formed during the reaction of sulfuric acid with iron and is a corrosion product on the surface of pipeline steel. The pH value, temperature, and time of exposure have a considerable influence on the formation of FeS [44–46].

Table 3. The volume fraction of ideal texture components and some important fibers in the Ref. and the heat-treated specimens.

Texture Components	Ref.	HT1	HT2	HT3
Cube	2.5	2.5	2.1	2.3
Goss	2	1.8	2.2	1.8
Brass	6.4	5.8	5.4	5.4
S	10.8	9.1	10.1	9.7
Copper	4.4	3.4	4.1	3.7
R-cube	1.5	1.6	1.7	1.6
γ {111} ‖ ND	9.2	9.7	10.8	11.6
Ratio gamma to R-cube	6.1	6.2	6.2	6.9
α {110} ‖ RD	9.6	8.8	9.3	8.5
{332} <113>	26.3	27.1	28.2	29.2

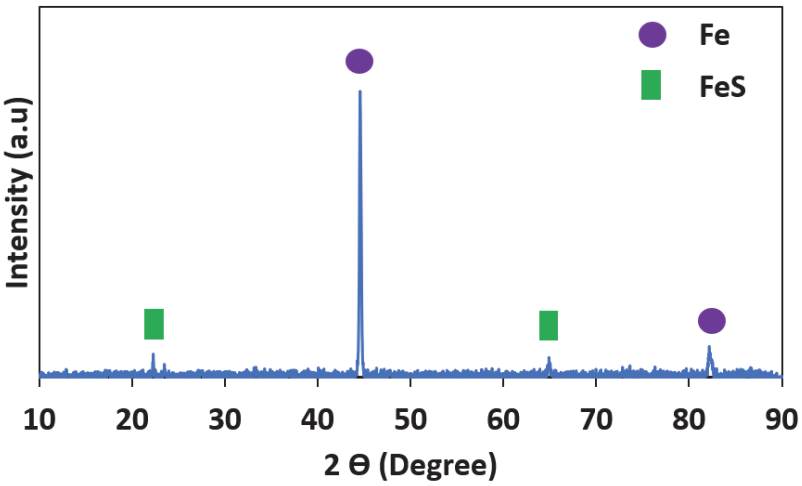

Figure 10. XRD analysis of corrosion products on the corroded surface.

Figure 11a–d show the SEM images of the corroded surface of the pipeline steels in the Ref., HT1, HT2, and HT3 specimens, respectively. In these images, uniform corrosion attacks were observed on the surface of all the corroded specimens and there was no obvious localized corrosion.

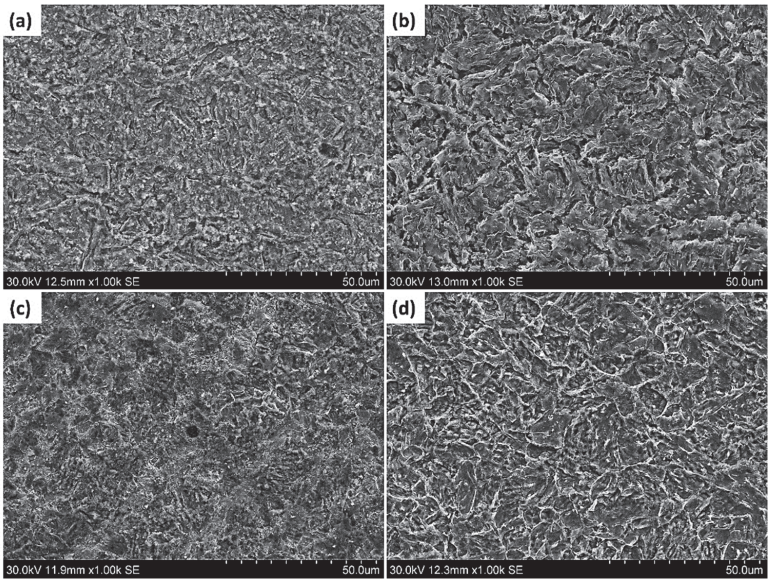

Figure 11. SEM images of the corroded surface of pipeline steels (**a**) Ref., (**b**) HT1, (**c**) HT2, and (**d**) HT3.

4. Conclusions

In this study, X100 pipeline steel (Ref.) specimens were subjected to three different austenitizing temperatures of 880 °C (for specimen HT3), 830 °C (for specimen HT2), and 780 °C (for specimen HT1) for 90 min followed by oil quenching. Afterward, all of the specimens were tempered at 600 °C for 30 min. Based on the results obtained, the following conclusions are made:

1. The HT2 specimen had the potential to retain a high impact toughness value even after hydrogen charging, indicating a higher amount of hydrogen embrittlement resistance. On the other hand, the Ref. and HT3 specimens with high hardness values showed higher hydrogen embrittlement susceptibility, indicating that the hydrogen embrittlement resistance decreased with increasing hardness values.
2. The corrosion test results indicate that the corrosion resistance of the Ref. and heat-treated specimens can be arranged in the following order: HT3 < Ref. < HT1 < HT2. This result originates from the crystallographic texture analysis, which indicates that the HT1 and HT2 steel with the optimum combination of advantageous texture components ({110}, {111},{332}) and harmful texture components ({100}) exhibited a superior level of corrosion resistance in the acidic environments.
3. The EBSD analysis of the KAM maps indicated that the HT3 and Ref. Please put here "Not applicable" have the highest amount of internally stored energy, resulting in the lowest corrosion resistance.

Author Contributions: Conceptualization, R.K.Z.D., J.F.A.C., S.Y. and M.A.M.-B.; methodology, R.K.Z.D., J.F.A.C., S.Y. and E.E.; formal analysis, R.K.Z.D., S.Y., E.E. and M.A.M.-B.; investigation, S.Y., J.F.A.C., R.K.Z.D. and E.E.; writing—original draft preparation, M.A.M.-B. and E.E.; writing—review and editing, E.E., R.K.Z.D., S.Y. and J.S.; supervision, J.S. All authors have read and agreed to the published version of the manuscript.

Funding: The research received no external funding.

Institutional Review Board Statement: Not applicable.

Informed Consent Statement: Not applicable.

Data Availability Statement: Data will be made available on request.

Acknowledgments: The authors acknowledge the support of the University of Saskatchewan.

Conflicts of Interest: The authors declare no conflict of interests.

References

1. Pourazizi, R.; Mohtadi-Bonab, M.A.; Zadeh Davani, R.K.; Szpunar, J.A. Effect of Thermo-Mechanical Controlled Process on Microstructural Texture and Hydrogen Embrittlement Resistance of API 5L X70 Pipeline Steels in Sour Environments. *Int. J. Press. Vessel. Pip.* **2021**, *194*, 104491. [CrossRef]
2. Entezari, E.; González-Velázquez, J.L.; López, D.R.; Zúñiga, M.A.B.; Szpunar, J.A. Review of Current Developments on High Strength Pipeline Steels for HIC Inducing Service. *Frat. Ed Integrità Strutt.* **2022**, *16*, 20–45. [CrossRef]
3. Sharma, L.; Chhibber, R. Microstructure Evolution and Electrochemical Corrosion Behaviour of API X70 Linepipe Steel in Different Environments. *Int. J. Press. Vessel. Pip.* **2019**, *171*, 51–59. [CrossRef]
4. González-Velázquez, J.L.; Entezari, E. On the Assessment of Non-Metallic Inclusions by Part 13 of API 579 -1/ASME FFS-1 2016. *Procedia Struct. Integr.* **2021**, *33*, 221–228. [CrossRef]
5. Kpemou, A.M.; Guy, P.; Julien, C. Influence of Hydrogen Embrittlement on Ductile–Brittle Transition Temperature Determined on Mini-Charpy Specimens Made in X65 Steel. *J. Fail. Anal. Prev.* **2021**, *21*, 2290–2304. [CrossRef]
6. Fassina, P.; Bolzoni, F.; Fumagalli, G.; Lazzari, L.; Vergani, L.; Sciuccati, A. Influence of Hydrogen and Low Temperature on Mechanical Behaviour of Two Pipeline Steels. *Eng. Fract. Mech.* **2012**, *81*, 43–55. [CrossRef]
7. Coseru, A.; Capelle, J.; Pluvinage, G. On the Use of Charpy Transition Temperature as Reference Temperature for the Choice of a Pipe Steel. *Eng. Fail. Anal.* **2014**, *37*, 110–119. [CrossRef]
8. Johnson, W.H., II. On Some Remarkable Changes Produced in Iron and Steel by the Action of Hydrogen and Acids. *Proc. R. Soc. London* **1875**, *23*, 168–179. [CrossRef]

9. Zhang, T.; Zhao, W.; Li, T.; Zhao, Y.; Deng, Q.; Wang, Y.; Jiang, W. Comparison of Hydrogen Embrittlement Susceptibility of Three Cathodic Protected Subsea Pipeline Steels from a Point of View of Hydrogen Permeation. *Corros. Sci.* **2018**, *131*, 104–115. [CrossRef]
10. Magnin, T. Mécanismes de Fatigue-Corrosion Des Alliages Métalliques. *Rev. Métallurgie* **2002**, *99*, 423–432. [CrossRef]
11. Steigerwald, E.A.; Schaller, F.W.; Troiano, A.R. The Role of Stress in Hydrogen Induced Delayed Failure. *Trans. Met. Soc. AIME* **1960**, *218*.
12. Gong, K.; Wu, M.; Liu, G. Comparative Study on Corrosion Behaviour of Rusted X100 Steel in Dry/Wet Cycle and Immersion Environments. *Constr. Build. Mater.* **2020**, *235*, 117440. [CrossRef]
13. Gong, K.; Wu, M.; Xie, F.; Liu, G.; Sun, D. Effect of Dry/Wet Ratio and PH on the Stress Corrosion Cracking Behavior of Rusted X100 Steel in an Alternating Dry/Wet Environment. *Constr. Build. Mater.* **2020**, *260*, 120478. [CrossRef]
14. Zhao, J.; Wang, S.; Gu, Y.; Xiong, D.; Tian, B. Microstructure and Corrosion Performance of X100 Steel in the Oilfield Produced Water. *Corros. Eng. Sci. Technol.* **2019**, *54*, 649–658. [CrossRef]
15. González Velázquez, J.L.; Entezari, E.; López, D.R.; Beltrán Zúñiga, M.A.; Szpunar, J. Experimental and In-Service Observations of HIC Nucleation and Growth in Pipeline Steel. In *49th Annual Review of Progress in Quantitative Nondestructive Evaluation*; American Society of Mechanical Engineers: New York, NY, USA, 2022; Volume 2022. [CrossRef]
16. Eliyan, F.F.; Alfantazi, A. Electrochemical Investigations on the Corrosion Behavior and Corrosion Natural Inhibition of API-X100 Pipeline Steel in Acetic Acid and Chloride-Containing CO2-Saturated Media. *J. Appl. Electrochem.* **2012**, *42*, 233–248. [CrossRef]
17. Dong, C.F.; Liu, Z.Y.; Li, X.G.; Cheng, Y.F. Effects of Hydrogen-Charging on the Susceptibility of X100 Pipeline Steel to Hydrogen-Induced Cracking. *Int. J. Hydrogen Energy* **2009**, *34*, 9879–9884. [CrossRef]
18. Pourazizi, R.; Mohtadi-Bonab, M.A.; Szpunar, J.A. Investigation of Different Failure Modes in Oil and Natural Gas Pipeline Steels. *Eng. Fail. Anal.* **2020**, *109*, 104400. [CrossRef]
19. Entezari, E.; Avishan, B.; Mousalou, H.; Yazdani, S. Effect of Electro Slag Remelting (ESR) on the Microstructure and Mechanical Properties of Low Carbon Bainitic Steel. *Kov. Mater* **2018**, *56*, 253–263. [CrossRef]
20. Pourazizi, R.; Mohtadi-Bonab, M.A.; Szpunar, J.A. Role of Texture and Inclusions on the Failure of an API X70 Pipeline Steel at Different Service Environments. *Mater. Charact.* **2020**, *164*, 110330. [CrossRef]
21. Entezari, E.; Mousalou, H.; Yazdani, S.; González-Velázquez, J.L.; Szpunar, J.A. The Evaluation of Quenching Temperature Effect on Microstructural and Mechanical Properties of Advanced High Strength Low Carbon Steel After Quenching Partitioning Treatment. *Procedia Struct. Integr.* **2022**, *37*, 145–152. [CrossRef]
22. Masoumi, M.; Silva, C.C.; Béreš, M.; Ladino, D.H.; de Abreu, H.F.G. Role of Crystallographic Texture on the Improvement of Hydrogen-Induced Crack Resistance in API 5L X70 Pipeline Steel. *Int. J. Hydrogen Energy* **2017**, *42*, 1318–1326. [CrossRef]
23. Fuchigami, H.; Minami, S.H.; Nagumo, M. Effect of Grain Size on the Susceptibility of Martensitic Steel to Hydrogen-Related Failure. *Philos. Mag. Lett.* **2006**, *86*, 21–29. [CrossRef]
24. Masoumi, M.; Silva, C.C.; de Abreu, H.F.G. Effect of Crystallographic Orientations on the Hydrogen-Induced Cracking Resistance Improvement of API 5L X70 Pipeline Steel under Various Thermomechanical Processing. *Corros. Sci.* **2016**, *111*, 121–131. [CrossRef]
25. Ohaeri, E.; Omale, J.; Tiamiyu, A.; Rahaman, K.M.M.; Szpunar, J. Influence of Thermomechanically Controlled Processing on Microstructure and Hydrogen Induced Cracking Susceptibility of API 5L X70 Pipeline Steel. *J. Mater. Eng. Perform.* **2018**, *27*, 4533–4547. [CrossRef]
26. Omale, J.I.; Ohaeri, E.G.; Szpunar, J.A.; Arafin, M.; Fateh, F. Microstructure and Texture Evolution in Warm Rolled API 5L X70 Pipeline Steel for Sour Service Application. *Mater. Charact.* **2019**, *147*, 453–463. [CrossRef]
27. Schreiber, A.; Rosenkranz, C.; Lohrengel, M.M. Grain-Dependent Anodic Dissolution of Iron. *Electrochim. Acta* **2007**, *52*, 7738–7745. [CrossRef]
28. Madrigal-Cano, M.; Hernández-Maya, L.; Hallen, J.M.; Corrales-Luna, M.; Arce-Estrada, E.M.; Le Manh, T. Model for the Correlation between Anodic Dissolution Resistance and Crystallographic Texture in Pipeline Steels. *Materials* **2018**, *11*, 1432. [CrossRef]
29. Ohaeri, E.; Omale, J.; Eduok, U.; Szpunar, J. Effect of Thermomechanical Processing and Crystallographic Orientation on the Corrosion Behavior of API 5L X70 Pipeline Steel. *Metall. Mater. Trans. A* **2018**, *49*, 2269–2280. [CrossRef]
30. Ohaeri, E.; Omale, J.; Eduok, U.; Szpunar, J.; Arafin, M.; Fazeli, F. Effect of Microstructure and Texture Evolution on the Electrochemical Corrosion Behavior of Warm-Rolled API 5L X70 Pipeline Steel. *Metall. Mater. Trans. Part A* **2020**, *51*, 2255–2275. [CrossRef]
31. Venegas, V.; Caleyo, F.; Baudin, T.; Espina-Hernández, J.H.; Hallen, J.M. On the Role of Crystallographic Texture in Mitigating Hydrogen-Induced Cracking in Pipeline Steels. *Corros. Sci.* **2011**, *53*, 4204–4212. [CrossRef]
32. Hoschke, J.; Chowdhury, M.F.W.; Venezuela, J.; Atrens, A. "A review of hydrogen embrittlement in gas transmission pipeline steels". *Corros. Rev.* **2023**. [CrossRef]
33. Roy, U.; McDowell, D.L.; Zhou, M. Effect of Grain Orientations on Fracture Behavior of Polycrystalline Metals. *J. Mech. Phys. Solids* **2021**, *151*, 104384. [CrossRef]
34. Mohtadi-Bonab, M.A.; Mousavi, H.; Pourazizi, R.; Szpunar, J.A. Finite Element Modeling of Hic Propagation in Pipeline Steel with Regard to Experimental Observations. *Int. J. Hydrogen Energy* **2020**, *45*, 23122–23133. [CrossRef]

35. Lee, S.-P.; Hwang, S.-K.; Lee, J.-K.; Son, I.-S.; Bae, D.-S. Effect of Hydrogen Charging on the Mechanical Properties of 304 Stainless Steels. *J. Korea Soc. Power Syst. Eng.* **2015**, *19*, 73–79. [CrossRef]
36. Huang, F.; Liu, J.; Deng, Z.J.; Cheng, J.H.; Lu, Z.H.; Li, X.G. Effect of Microstructure and Inclusions on Hydrogen Induced Cracking Susceptibility and Hydrogen Trapping Efficiency of X120 Pipeline Steel. *Mater. Sci. Eng. A* **2010**, *527*, 6997–7001. [CrossRef]
37. Peng, Z.; Liu, J.; Huang, F.; Zhang, S.; Hu, Q.; Wang, Z.; Wang, Y. The Significance of Inclusion Morphology and Composition in Governing Hydrogen Transportation and Trapping in Steels. *Int. J. Hydrogen Energy* **2021**, *46*, 28811–28822. [CrossRef]
38. Moon, J.; Kim, S.-J.; Lee, C. Role of Ca Treatment in Hydrogen Induced Cracking of Hot Rolled API Pipeline Steel in Acid Sour Media. *Met. Mater. Int.* **2013**, *19*, 45–48. [CrossRef]
39. Latifi, A.; Miresmaeili, R.; Abdollah-Zadeh, A. The Mutual Effects of Hydrogen and Microstructure on Hardness and Impact Energy of SMA Welds in X65 Steel. *Mater. Sci. Eng. A* **2017**, *679*, 87–94. [CrossRef]
40. Fouda, A.S.; El-Ewady, G.; Ali, A.H. Modazar as Promising Corrosion Inhibitor of Carbon Steel in Hydrochloric Acid Solution. *Green Chem. Lett. Rev.* **2017**, *10*, 88–100. [CrossRef]
41. Santoso, R.P.; Riastuti, R. Corrosion Evaluation of Heat Recovery Steam Generator Superheater Tube in Two Methods of Testing: Tafel Polarization and Electrochemical Impedance Spectroscopy (EIS). In *AIP Conference Proceedings*; AIP Publishing LLC: Melville, NY, USA, 2018; Volume 1964, p. 20023.
42. Santos, B.A.F.; Serenario, M.E.D.; Souza, R.C.; Oliveira, J.R.; Vaz, G.L.; Gomes, J.; Bueno, A.H.S. The Electrolyte Renewal Effect on the Corrosion Mechanisms of API X65 Carbon Steel under Sweet and Sour Environments. *J. Pet. Sci. Eng.* **2021**, *199*, 108347. [CrossRef]
43. Mohtadi-Bonab, M.A.; Eskandari, M.; Szpunar, J.A. Texture, Local Misorientation, Grain Boundary and Recrystallization Fraction in Pipeline Steels Related to Hydrogen Induced Cracking. *Mater. Sci. Eng. A* **2015**, *620*, 97–106. [CrossRef]
44. Shi, F.; Zhang, L.; Yang, J.; Lu, M.; Ding, J.; Li, H. Polymorphous FeS Corrosion Products of Pipeline Steel under Highly Sour Conditions. *Corros. Sci.* **2016**, *102*, 103–113. [CrossRef]
45. Tang, J.; Shao, Y.; Zhang, T.; Meng, G.; Wang, F. Corrosion Behaviour of Carbon Steel in Different Concentrations of HCl Solutions Containing H2S at 90 °C. *Corros. Sci.* **2011**, *53*, 1715–1723. [CrossRef]
46. Li, Y.; van Santen, R.A.; Weber, T. High-Temperature FeS–FeS2 Solid-State Transitions: Reactions of Solid Mackinawite with Gaseous H2S. *J. Solid State Chem.* **2008**, *181*, 3151–3162. [CrossRef]